ACS APPLIED POLYMER MATERIALS

pubs.acs.org/acsapm Article

Aqueous Two-Phase System Enabled Dual-Layered Hydrogels with Tunable Nanoparticle Localization

Aniruddha Kambekar, Vignesh Nandhagopal, Aditya Mehta, Yashwant Kumar, Reman Kumar Singh, and Karthik Pushpavanam*

Cite This: *ACS Appl. Polym. Mater.* 2025, 7, 10062−10073 Read Online

ACCESS | Metrics & More | Article Recommendations | Supporting Information

ABSTRACT: Hydrogels are cross-linked polymeric networks capable of absorbing large amounts of water and have been widely explored for applications in drug delivery, tissue engineering, biosensing, and environmental remediation. The recent development of dual-layered hydrogels (DLHs) has expanded their potential, enabling spatial control over their mechanical and chemical properties. Furthermore, incorporating nanoparticles into each of these layers introduces unique optical, electronic, or catalytic properties, expanding the scope of these materials. However, complex processes often hinder the fabrication of DLHs, requiring precise control over the reaction conditions. This poses challenges in achieving a uniform nanoparticle distribution without aggregation. This work presents an approach for synthesizing DLHs with an aqueous two-phase system (ATPS), integrating phase separation and selective nanoparticle localization, followed by subsequent polymerization. Using a model system of poly(ethylene glycol) (PEG) and dextran (DEX) to generate the ATPS, we combined acrylamide, bis(acrylamide), and Irgacure (photoinitiator) to fabricate DLHs. Rheological studies provided insights into the viscoelastic behavior of DLHs, while mercury porosimetry was employed to analyze the pore size distribution. We illustrate that citrate-capped gold nanoparticles can be localized within the PEG-rich layer, while bovine serum albumin (BSA)-capped silver nanoparticles can be localized within the DEX-rich layer. We performed molecular dynamics simulations to investigate the factors contributing to the preferential partitioning. Finally, we exploit the fabricated DLHs with localized nanoparticles to catalyze the conversion of *p*-nitrophenol to *p*-aminophenol in the presence of gold nanoparticles. Upon laser irradiation at 450 nm, the reaction rate is further enhanced due to photothermal heating induced by the silver nanoparticles. We anticipate that this process offers a fabrication route toward multifunctional DLHs with spatially organized nanoparticles, opening avenues for advanced catalytic and responsive materials.

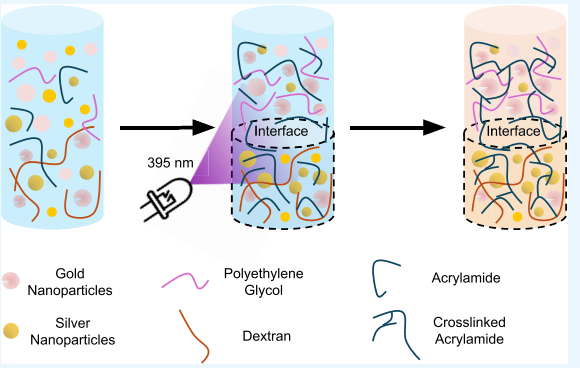

KEYWORDS: *aqueous two-phase system, gold nanoparticles, silver nanoparticles, dextran, polyethylene glycol, hydrogel, photothermal*

INTRODUCTION

Hydrogels are cross-linked polymeric networks fabricated through covalent, ionic, or physical cross-links capable of absorbing significant amounts of water (>90% by weight).[1] These hydrogels exhibit high porosity, tunable mechanical strength, and environmental responsiveness, making them ideal candidates for diverse applications, including but not limited to drug delivery, tissue engineering, biosensing, and environmental remediation.[2] While hydrogels are effective as standalone materials, their functionality and application scope are significantly enhanced by incorporating additives. For instance, polysaccharides such as chitosan and alginate improve biocompatibility and biodegradability.[3] Microparticles have been incorporated to promote the intended cellular responses.[4] Amphiphilic molecules forming micelles have been integrated within hydrogels to enable controlled release of biologics for therapeutic purposes.[1,5] Nanofibers are embedded within hydrogels to mimic extracellular matrix structures and form tissue-engineered scaffolds.[6] Quantum dots, known for their fluorescence imaging capabilities, have been integrated to facilitate real-time tracking of hydrogel behavior in biomedical applications.[7] Expanding the scope of hydrogel modifications, integrating nanoparticles introduces unique attributes to hydrogels, which amplify their capabilities and extend their application range in medicine, electronics, energy, and environmental sciences.[8−10]

Received: May 16, 2025
Revised: July 10, 2025
Accepted: July 11, 2025
Published: July 19, 2025

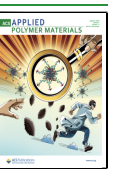

https://doi.org/10.1021/acsapm.5c01687
ACS Appl. Polym. Mater. 2025, 7, 10062−10073

Building on these needs, there has been a focus on precise nanoparticle localization within hydrogel matrices. Dual-layered hydrogels (DLHs) exemplify this approach, with each layer designed to contain a specific type of nanoparticle tailored to distinct tasks. Feng et al. developed a DLH with a light-to-heat conversion layer (LHL) containing polydopamine-manganese nanoparticles and a water absorption layer (WAL) containing 2-(acryloyloxyethyl)trimethylammonium chloride for atmospheric moisture harvesting. The LHL enabled photothermal water release, while the WAL ensured high water absorption capacity.[11] Alternatively, sequentially integrated DLHs were designed to enhance solar-driven hydrogen production.[12] The upper layer incorporated a platinum/titanium oxide (Pt/TiO_2) cryoaerogel, known for its photocatalytic efficiency in hydrogen evolution reactions. In contrast, the lower layer contained single-atom copper/titanium dioxide ($Cu\text{-}SA/TiO_2$) nanoparticles, where Cu-SA sites on TiO_2 serve as active centers to boost the photocatalytic activity. This configuration facilitated efficient charge separation and light absorption, significantly enhancing hydrogen production under solar irradiation.[12]

Dual-layered hydrogels (DLHs) are typically formed using multistep processes that rely on sequential polymerization, diffusion-driven cross-linking, or phase separation.[13] The common approach involves casting a prepolymer solution for the first layer, polymerizing it, and then adding a second prepolymer solution on top and curing it separately to form a layered structure.[14] For instance, a solution composed of acrylamide, acrylic acid, PEGDA, and α-ketoglutaric acid was first UV-cured to form the inner layer. Subsequently, a second solution containing *N*-isopropylacrylamide (NIPAM), acrylic acid, PEGDA, and graphene dispersion was cast on top and UV-cured to form the outer layer to achieve a DLH.[15] Another strategy uses diffusion-based initiation across layers. Here, a physically cross-linked core hydrogel composed of sodium alginate (SA) and carboxymethyl cellulose (CMC) was first formed by dropping the mix into $CaCl_2$ with ammonium persulfate (APS).[16] APS diffused outward to initiate chemical cross-linking of an outer layer composed of acrylic acid (AA) and *N*,*N*-dimethylacrylamide (DMAA), using *N*,*N*′-methylenebis(acrylamide) (MBAm) as a cross-linker.[17] This formed a pH-sensitive, drug-releasing double-layer structure with distinct inner (SA−CMC) and outer (PAA−PDMAA) layers.[18] A third strategy leverages aqueous two-phase systems, where a mixture of PEG 8000 and dextran T40 was prepared in the two-phase regime, allowing spontaneous separation into PEG-rich (top) and DEX-rich (bottom) layers. Upon equilibrium, acrylamide (10 wt %) and cross-linkers (MBAA, 0.5 wt %) were added and UV-cured, yielding a dual-layered hydrogel.[19] Despite the remarkable progress in DLH fabrication, these methods are inherently multistep or have not demonstrated the localization of nanoparticles within the distinct layers of the DLHs. There is a pressing need to develop methods to enable their broader adoption and practical application in various fields.

In this work, we present an approach that integrates phase separation into dual layers along with specific nanoparticle localization in each layer, followed by polymerization, to fabricate dual-layered hydrogels (DLHs). Unlike conventional methods that typically require multiple steps (layer-by-layer assembly) to form distinct hydrogel layers and incorporate functional components, our strategy significantly reduces the complexity of the synthesis, offering a more efficient route to fabricating DLHs.

MATERIALS AND METHODS

Materials. Polyethylene Glycol 8000 (PEG) for molecular biology (CAS Number: 25322-68-3), Dextran 70000 (DEX) from *Leuconostoc* spp. (CAS Number: 9004-54-0), and acrylamide/bis(acrylamide) (AA/BisAA) 30% solution (29:1 Ratio) (MDL number: MFCD00080848) were purchased from Sisco Research Laboratories Pvt., Ltd. Ammonium persulfate (APS) (CAS Number: 7727-54-0) was purchased from Finar Chemicals. Irgacure 2959 (CAS Number106797-53-9) was purchased from TCI Chemicals. Bovine serum albumin (CAS Number: 9048-46-8) was purchased from HiMedia Laboratories. Sodium borohydride (CAS Number: 16940-66-2), Polyethylene Glycol 400 (PEG 400) (CAS Number: 25322-68-3), trisodium citrate dihydrate (CAS Number: 6132-04-3), and silver nitrate (CAS Number: 7761-88-8) were purchased from Sigma-Aldrich. 4-Nitrophenol (CAS Number: 100-02-7) was purchased from Spectrochem Pvt., Ltd. UV LED Flood Light (395 nm, 36 W) was purchased from RDR Innovations. Milli-Q water was used as the solvent unless otherwise indicated.

Generation of Binodal Curve via the Cloud-Point Method. Stock solutions of 40 wt % PEG and 40 wt % DEX were prepared. For the binodal curve determination, different concentrations of PEG and DEX were systematically mixed and vortexed for 30 s. The cloud point was determined visually by observing the transition from a transparent solution to turbid. The concentrations of PEG and DEX where turbidity was observed were recorded. The critical binodal points were identified by narrowing the concentration range iteratively, which enabled precise mapping of the binodal curve.

Generation of PEG and DEX Aqueous Two-Phase System and Dual-Layered Hydrogels. Four distinct aqueous two-phase systems (ATPS) were synthesized with varying compositions of poly(ethylene glycol) (PEG) and dextran (DEX): ATPS-1 comprised 10% PEG 8000 and 4% DEX, ATPS-2 contained 8% PEG 8000 and 8% DEX, ATPS-3 included 4% PEG 8000 and 12% DEX, and ATPS-4 consisted of 8% PEG 400 and 8% DEX. For the generation of ATPS-1, in a 500 μL microcentrifuge tube (MCT), 32.5 μL of 30.8 wt % PEG stock solution, 24.8 μL of 16.1 wt % DEX stock solution, and 43.2 μL of Milli-Q water were added. For the generation of ATPS-2, in a 500 μL MCT, 28.4 μL of 28.3 wt % PEG stock solution, 28.4 μL of 28.3 wt % DEX stock solution, and 43.2 μL of Milli-Q water were added. For the generation of ATPS-3, in a 500 μL MCT, 26.5 μL of 15.1 wt % PEG stock solution, 34.5 μL of 34.8 wt % DEX stock solution, and 43.2 μL of Milli-Q water were added. For the generation of ATPS-4, in a 500 μL MCT, 28.4 μL of 28.3 wt % PEG 400 stock solution, 28.4 μL of 28.3 wt % DEX stock solution, and 43.2 μL of Milli-Q water were added. The mixture was vortexed thoroughly for 30 s to achieve homogeneity. Subsequently, the tube was centrifuged at 60 rpm for 1 min. At the end of the process, an aqueous two-phase system was formed with a clear interface observed between the two phases. To fabricate the DLHs, 43.2 μL of Milli-Q water was replaced with 33.2 μL of acrylamide/bis(acrylamide). The mixture was vortexed thoroughly for 30 s to achieve homogeneity. The mixture was then centrifuged at 60 rpm for 1 min. Following centrifugation, 10 μL of 50 wt % Irgacure was carefully added from the top without disturbing the interface of the ATPS. The mixture was subsequently placed in front of a UV LED flood light (395 nm, 36 W), and varying durations of light exposure were tested. A 2 h exposure was determined to be sufficient for forming DLHs.

Field-Emission Scanning Electron Microscopy (FE-SEM). The DLHs were sectioned along the vertical cross-sectional plane and lyophilized. The nonconductive DLHs were subsequently coated with platinum for 90 s before imaging. Scanning electron micrographs were acquired by FE-SEM (Jeol JSM7600F).

Rheological Characterization. Cylindrical DLHs (diameter 8 mm, height 3 mm) were fabricated in the cap of a 2 mL MCT. The samples were shipped to IIT Madras, India, for rheological characterization. To prevent dehydration during transportation, 100

https://doi.org/10.1021/acsapm.5c01687
ACS Appl. Polym. Mater. 2025, 7, 10062−10073

μL of Milli-Q water was added to each tube. The rheological properties of the DLHs were examined using an Anton Paar Physica 301 rheometer with a parallel plate with an 8 mm diameter and at a measuring gap of 2 mm between the plates. Amplitude sweep measurements were performed by varying the strain amplitude over a 0.1−100% range at a constant angular frequency of 1 rad/s. Frequency sweep measurements were performed by varying the angular frequency over a 0.1 to 100 rad/s range at a constant strain amplitude of 0.5%, in the linear viscoelastic region limit. A three-loop thixotropy test (3iTT) was performed at two different strain amplitudes, 0.5 and 100%, corresponding to both linear and nonlinear regions, respectively, to understand the recovery ability of the gels.

Mercury Intrusion Porosimetry (MIP) Analysis. The DLHs were lyophilized and shipped to IIT Madras, India. The porosity of DLHs was measured using mercury intrusion porosimetry (Microtrac Mercury Porosimeter). The Pascal stepwise pressure increase and decrease method was employed, with a pressure ramp rate of 8−35 MPa/min and a maximum test pressure of 280 MPa. All measurements were performed at a constant temperature of 30 °C. However, it is acknowledged that high-pressure mercury intrusion may still introduce compression artifacts.

Fourier Transform Infrared Spectroscopy (FTIR) Analysis. FTIR spectra were recorded using a PerkinElmer FTIR spectrophotometer across the spectral range of 4000−500 cm^{-1}, to investigate the spectra of PEG, DEX, ATPS, PEG-rich layer, and DEX-rich layer.

Synthesis of Citrate-Capped Gold Nanoparticles. The Turkevich method was employed to synthesize citrate-capped gold nanoparticles.[20] Briefly, 20 mL of a 1 mM aqueous chloroauric acid ($HAuCl_4$) solution was heated to a boil under constant stirring. Upon reaching the boiling point, 2 mL of 1 wt % sodium citrate dihydrate solution was rapidly added as a reducing and stabilizing agent. The deep-red-colored gold nanoparticles synthesized were characterized using absorbance measurement.

Synthesis of Bovine Serum Albumin (BSA)-Capped Silver Nanoparticles. 63 mg of silver nitrate was dissolved in 8 mL of Milli-Q water, and 200 mg of BSA was added. The solution was further supplemented with 2 mL of sodium borohydride ($NaBH_4$) stock (7 mg/mL) and stirred vigorously for 30 min. The resulting brown-colored silver nanoparticles were collected through centrifugation (10,000 rpm, 10 min), washed with Milli-Q water, and resuspended in 10 mL of Milli-Q water.[21]

Transmission Electron Microscopy. The samples of citrate-capped gold nanoparticles were prepared by drop-casting the nanoparticles onto 300 mesh copper grids, followed by drying under a vacuum. The samples of BSA-capped silver nanoparticles were prepared by drop-casting the nanoparticles onto 300 mesh copper grids; then, the samples underwent ozone cleaning for 15 min, followed by drying under vacuum. Transmission electron micrographs were acquired on FEI, Themis 60−300 with an EDS detector and FEI-Ceta 4k × 4k camera. ImageJ software was used to determine the size of the nanoparticles.

Zeta Potential Measurements. Zeta potential measurements for the citrate-capped gold nanoparticles (~3.6×10^{12} nanoparticles/mL) and BSA-capped silver nanoparticles (~1.4×10^{15} nanoparticles/mL) were performed on Nano ZS (Malvern Instruments). Zeta potential was calculated with Malvern Zetasizer Nano ZS software.

Nanoparticle Leaching Study. To evaluate the leaching behavior of citrate-capped gold nanoparticles and BSA-capped silver nanoparticles from the DLHs, the DLHs were immersed in 250 μL of Milli-Q water. At predetermined time intervals of 2, 6, 12, and 24 h, the supernatant was collected and analyzed using UV−vis absorption spectroscopy (BioTek Cytation 5 microplate reader) to detect the presence and concentration of leached nanoparticles.

Dye Degradation Study. The catalytic reduction of *p*-nitrophenol to *p*-aminophenol was evaluated by using DLHs containing citrate-capped gold nanoparticles and BSA-capped silver nanoparticles. A freshly prepared solution of *p*-nitrophenol (0.22 mM) and sodium borohydride (11.1 mM) in a total volume of 200 μL was added to a 96-well microplate, and DLH was added to initiate the catalytic reaction. A control reaction without DLH was also included. At defined time intervals, the DLH was removed, and the absorbance of the solution was recorded using a BioTek Cytation 5 microplate reader. In a subsequent experiment, the same reaction setup was irradiated with a 450 nm laser (Shanghai Laser and Optics Century Co., Ltd.) to heat the BSA-capped silver nanoparticles embedded in the DEX-rich layer locally. The reaction kinetics were analyzed using a pseudo-first-order model, and the rate constant (k) was calculated from the slope of the $\ln(A/A_0)$ versus time (min) plot.

Biocompatibility Studies. Human breast cancer cells (MDA-MB-231) were cultured in DMEM high-glucose medium supplemented with 10% fetal bovine serum (FBS) and 1% penicillin−streptomycin solution in T-25 flasks. The cells were maintained in a CO_2 incubator at 37 °C with 5% CO_2. The cytotoxicity of the DLHs was assessed by using the MTT assay. Briefly, 100 μL of a cell suspension (5×10^3 cells) was seeded into each well of a 96-well microplate and incubated for 24 h. Following this, the media were aspirated and replaced with DLH-treated media, and cells were incubated for an additional 24 h. After treatment, 100 μL of MTT solution (0.5 mg/mL) was added to each well and incubated for 4 h at 37 °C. The MTT solution was removed, and the resulting formazan crystals were solubilized with 100 μL of DMSO. Absorbance was measured at 590 nm using a BioTek Cytation 5 plate reader. Cell viability was calculated using the formula:

$$\%\text{cell viability} = \frac{Ab_s}{Ab_c} \times 100$$

Ab_s and Ab_c represent the absorbances of the treated and control samples, respectively, at 590 nm.

Molecular Dynamics Simulations of Polymer−Protein and Polymer−Nanoparticle Interactions. Coarse-grained methodology was used to simulate the DEX-BSA and PEG-BSA systems. All-atom methodology was utilized for the gold nanoparticle-DEX and gold nanoparticle-PEG systems. The details of the system setups and simulation protocols are given below.

Coarse-Grained Simulations. The all-atom structures of BSA were taken from the AlphaFold Structure Database.[22] The 8000 Da DEX model and PEG were built using polyply1.0.[23] Atoms were coarse-grained to the ELNEDIN model using the martinize2 tool and martini3001 ForceField parameters.[24−26] In the initial configurations of both the DEX-BSA and PEG-BSA systems, the polymer chains were positioned to maintain a minimum distance of approximately 1.6 nm from the protein. The Martini3 standard water model was used to solvate the system. The system was neutralized with the addition of Na^+ counterions. Energy minimization was carried out using the steepest descent algorithm for 50,000 steps. Then, equilibration was carried out in a single step with NVT and NPT using a V-rescale thermostat to maintain 300 K and a Berendsen barostat with isotropic pressure coupling to achieve 1 atm for 20 ns, respectively.[27,28] Finally, a 3 μs production run was carried out at constant temperature (300 K) and pressure (1 atm), using a V-rescale thermostat and a Parrinello−Rahman barostat, respectively.[29] All the simulations were carried out using GROMACS software 2021.3 version.[30] During the simulation, the nonbonded cutoff was set to 1.1 nm. All the bonds were constrained using the LINCS algorithm.[31]

All-Atom Molecular Simulations. The bare gold spherical nanoparticle with a radius of 2.8 nm was modeled using the CHARMM-GUI Nanomaterial Modeler.[32−35] PEG (~8000 Da) was modeled using the Polymer builder (system type: solution), while DEX (~8000 Da) was modeled using the Glycan Modeler (CHARMM36 Force field) in CHARMM-GUI.[36−39] Due to the linear nature of the DEX model, simulated annealing was employed to obtain its equilibrated minimum-energy conformation.[40] MD simulations were carried out using GROMACS software 2021.3 version.[30] The TIP3P water model was used for the solvation.[41] No ions were added since the systems were neutral. Systems were energy minimized using the steepest descent for 50,000 steps.[41] The nonbonded cutoff of about 1.2 nm and the potential shift from 1.0 to 1.2 nm was used to get a smooth potential shift. The system was equilibrated in two steps, NVT and NPT: to maintain the

https://doi.org/10.1021/acsapm.5c01687
ACS Appl. Polym. Mater. 2025, 7, 10062−10073

experimental temperature of 300 K with the V-rescale thermostat with coupling constant 1 ps for 2 ns[27] and to handle long-range interactions with the Particle Mesh Ewald algorithm (PME).[42] NPT was carried out using Berendsen barostat to achieve 1 atm with a coupling constant of 2 ps for 10 ns.[28] The LINCS algorithm was used to constrain the bonds.[31] Production runs were performed for 80 ns at constant temperature (300 K) and constant pressure (1 bar) using the V-rescale thermostat and the Parrinello−Rahman barostat, respectively.

Trimer simulations of PEG and DEX were also performed using the same protocol with the deprotonated monocitrate molecule. The PEG trimer was modeled using the Polymer builder (system type: solution), while the DEX trimer was modeled using the Glycan Modeler (CHARMM36 Force field) in the CHARMM-GUI, respectively.[36−39] Following 1 ns of NVT and 10 ns of NPT equilibration, production runs were carried out for 80 ns using the same thermostat and barostat settings as mentioned.

Analysis of MD Simulations. To quantify the interactions, we calculated the number of contacts with a 0.45 nm cutoff from BSA and gold nanoparticle surfaces. Interaction energy and number of contacts were averaged over the last 200 ns (i.e., from 2800 to 3000 ns) for BSA systems and the last 5 ns of the production run (i.e., from 75 to 80 ns) for gold nanoparticle systems.

RESULTS AND DISCUSSION

Aqueous two-phase systems (ATPS) consist of two immiscible aqueous phases formed by a combination of polymers, salts, or surfactants, resulting in a distinctive environment that promotes phase separation.[7] These systems have also demonstrated their versatility in nanomaterial separation and synthesis. For instance, DNA-coated single-walled carbon nanotubes (SWCNTs) have been effectively partitioned into 15 distinct chiral species within an ATPS, based on the DNA sequence, salts, and polymers employed.[43] This selective separation is attributed to the sensitivity of solvation energy.[43] Similarly, a polyethylene glycol and trisodium citrate-based ATPS has enabled the simultaneous synthesis and separation of silver nanoparticles, with the nanoparticles adsorbing at the interphase.[44] ATPS has been employed for the preferential localization of enzymes, such as lipases and peroxidases, within a specific phase.[45,46] This selective partitioning facilitates an improved enzyme recovery. These diverse applications of ATPS highlight its potential as a versatile platform for developing advanced materials. Building on these insights, we propose leveraging the spontaneous phase separation in ATPS, followed by nanoparticle localization within each phase, and then conducting *in situ* polymerization to generate dual-layered hydrogels (DLHs). This approach offers several advantages: it significantly reduces the fabrication time and simplifies the protocol by eliminating multistep processes.

We investigated the polyethylene glycol/dextran (PEG 8000/DEX 70,000) ATPS as the model system to demonstrate the continuous DLH fabrication process, wherein phase separation and polymerization occur in succession (Figure 1A). We employed the cloud-point method to establish the binodal curve, which delineates the boundary between the two- and single-phase regions (Figure 1B). To enhance the visualization of the single-phase and two-phase regions, we incorporated acid violet dye into the polymer mixture. Below the binodal curve, the solution remained homogeneous, as indicated by the uniform color distribution. Conversely, two distinct phases are formed above the binodal curve, marked by a clear color gradient due to the preferential localization of the dye. The PEG-rich layer forms the upper layer, while the DEX-rich layer forms the lower layer due to density differences.[43,45]

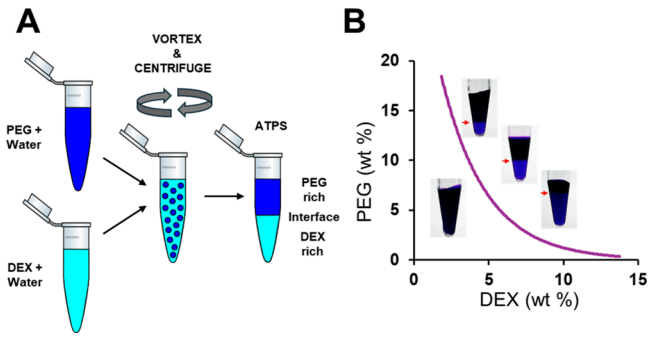

Figure 1. Formation and phase diagram of the PEG 8000/DEX 70,000 aqueous two-phase system (ATPS). (A) Schematic representation of the process involved in the generation of the PEG 8000/DEX 70,000 aqueous two-phase system (ATPS). PEG and DEX solutions are first prepared and then combined to achieve the desired concentrations. The mixture is vortexed thoroughly and subjected to centrifugation, resulting in phase separation. This process forms a clear interface, producing two distinct phases: a PEG-rich top phase and a DEX-rich bottom phase. (B) Binodal curve for the PEG 8000/DEX 70,000 aqueous two-phase system established using the cloud-point method. The solid purple line represents the boundary between the two-phase region (above the curve) and the single-phase region (below the curve).

Furthermore, we demonstrated that the relative volumes of the two phases could be adjusted by varying the concentrations of PEG and DEX in ATPS (Figure 1B inset).

To generate the DLHs through this approach, we mixed 8% each of PEG and DEX, which resulted in an approximately equal volumetric partition in two distinct layers (Figure 1B). To polymerize the phase-separated PEG and DEX systems, we added acrylamide/bis(acrylamide) (AA/BisAA) to a final concentration of 10%. This was followed by the addition of ammonium persulfate (APS) at 0.1 and 5% separately as a free-radical polymerization initiator. There was no noticeable hydrogel formation at 0.1% APS, while at 5% APS, successful polymerization was achieved (Figure S1A,B). Both layers of the resulting DLH exhibited distinct appearances. The top PEG-rich phase was milky white, while the bottom DEX-rich phase was transparent (Figure S1C).

We demonstrated that the approach of fabricating DLH through ATPS could be utilized to localize nanoparticles in one phase over the other. To show this, we synthesized citrate-capped gold nanoparticles and characterized them. The diameter and zeta potential of the citrate-capped gold nanoparticles determined through TEM and zeta analyzer were 17.06 ± 1.27 nm (Figure S2) and −35.3 ± 1.8 mV, respectively. After adding citrate-capped gold nanoparticles to the PEG-DEX ATPS system, we noticed a clear visual separation of the citrate-capped gold nanoparticles in the PEG-rich phase compared with the DEX-rich phase (Figure 2A). We further quantified the presence of gold nanoparticles in each phase through UV−visible spectroscopy by monitoring the absorbance at 520 nm, which is characteristic of gold nanoparticles (Figure 2B). While the characteristic absorbance peak appears in the PEG-rich phase, it is minimal in the DEX-rich phase, indicating the preference of citrate-capped gold nanoparticles toward the PEG-rich phase. The partition coefficient, defined as the ratio of absorbance in the PEG-rich phase to that in the DEX-rich phase, was 6.12. There was no evidence of aggregation, as indicated by the absence of any wavelength shift, validating the stability of the nanoparticles in

https://doi.org/10.1021/acsapm.5c01687
ACS Appl. Polym. Mater. 2025, 7, 10062−10073

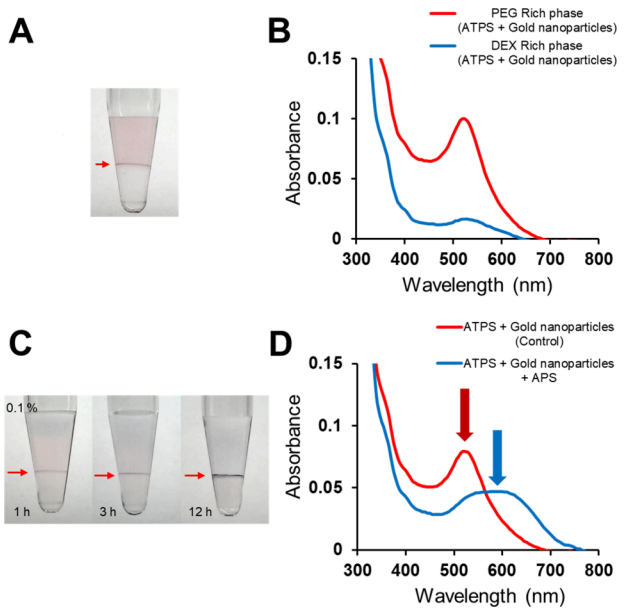

Figure 2. Accumulation and aggregation of gold nanoparticles in ATPS: visual and spectroscopic analysis. (A) Digital images reveal an accumulation of gold nanoparticles in the PEG-rich phase (above the interface) and minimal presence of gold nanoparticles in the DEX-rich phase (below the interface). This is evidenced by the pink coloration of the solution in the PEG-rich phase, contrasting with the absence of such a coloration in the DEX-rich phase. The red arrow indicates the position of the interface. (B) UV−visible spectroscopy analysis of gold nanoparticles in the PEG-rich phase and DEX-rich phase indicates a preferential accumulation of gold nanoparticles in the PEG-rich phase. (C) Digital images of ATPS containing gold nanoparticles and 0.1% APS show clear aggregation of gold nanoparticles, evidenced by a color change from pink to purple. (D) UV−visible spectroscopy analysis of gold nanoparticles upon addition of APS displays a shift in the absorbance peak indicative of gold nanoparticle aggregation.

the PEG-rich phase. Additionally, by modulating the weight percentages of PEG (10 and 4%) and DEX (4 and 12%), we could modulate the volume partition of the PEG-rich and DEX-rich phases. Even under these conditions, the gold nanoparticles visibly preferred the PEG-rich phase over the DEX-rich phase (Figure S3).

After achieving nanoparticle distribution in the PEG-rich phase, we incorporated 0.1% APS into the system. A clear visible color shift from pink to purple, indicative of gold nanoparticle aggregation, was noticeable (Figure 2C). This is also corroborated through UV−visible spectroscopy analysis, where there is a noticeable shift in the excitation maxima from 520 to 590 nm (Figure 2D). The instability of the gold nanoparticles upon addition of APS is likely due to the interaction between the negatively charged citrate-capped nanoparticles and the ammonium ions (NH_4^+) from APS. The positively charged ammonium ions reduce the electrostatic repulsion between the nanoparticles, which is essential for maintaining colloidal stability. This leads to closer particle proximity, overcoming repulsive forces and facilitating aggregation, as reflected in the observable spectral and visual changes.[47,48] Considering this, we selected Irgacure, a widely recognized photoinitiator used in free-radical polymerization. The rationale behind this substitution is that Irgacure does not contain ionizable moieties, unlike APS. It is therefore less likely to disrupt the electrostatic stability of the citrate-capped gold nanoparticles, thus minimizing the risk of aggregation.[49]

Before incorporating gold nanoparticles into the system containing irgacure, preliminary studies were conducted to optimize the polymerization conditions and ensure the formation of stable DLH. The PEG and DEX concentrations were fixed at 8%, with AA/BisAA (30%) at a final concentration of 10%. This is further supplemented with irgacure at 1 or 5% concentrations in the presence of UV light as polymerization photoinitiator (Figure S4). The polymerization process was observed to initiate in the DEX-rich phase and gradually propagate to the PEG-rich phase, enabling polymerization in both phases while preserving the interface. This phenomenon is likely attributed to the hydroxyl groups on dextran's glucopyranose residues, which can form hydrogen bonds with Irgacure.[50,51] Consequently, Irgacure exhibits a higher affinity for the DEX-rich phase, leading to the preferential initiation of polymerization. Successful polymerization occurred at 1 and 5% Irgacure (Figure S5 and Figure 3A). We demonstrate the optical characteristics of the fabricated DLH by positioning the DLH in front of a printed background with the repeating text "a". The PEG-rich layer of the hydrogel, characterized by its opacity, effectively obscured the text behind it, while the DEX-rich layer remained transparent, allowing the underlying text to be clearly visible through the hydrogel (Figure 3B). We used scanning electron microscopy to examine the nature of the pores in the DLHs formed within the ATPS hydrogels generated with two different AA/BisAA concentrations, 5 and 10% (Figure 3C and Figure S6).

Mercury intrusion porosimetry analysis was conducted to determine the porosity of the PEG-rich layer and the DEX-rich layer for three different DLHs (DLH-1: PEG 8000 (10%) - DEX (4%), DLH-2: PEG 8000 (8%) - DEX (8%), and DLH-3: PEG 8000 (4%) - DEX (12%)). Differential intrusion curves were plotted to analyze the pore size distribution (Figures S7A−R). A clear trend observed from DLH-1 to DLH-3 is the progressive increase in the total pore volume of the DEX-rich phase, while the PEG-rich phase exhibits a relatively constant pore volume (Figure 3D). This suggests that increasing the DEX concentration leads to the formation of a greater number of pores, likely due to a denser network of entangled DEX chains.[52] In contrast, variations in PEG concentration have a minimal impact on the total pore volume of the PEG-rich phase. This is likely due to the limited solubility between PEG and AA/BisAA, which may hinder the uniform network formation. This insolubility is also visually apparent, as the PEG-rich layer appears white (indicative of insolubility), unlike the transparent DEX-rich hydrogel. Additionally, the average pore diameter in the DEX-rich region decreases slightly with increasing DEX concentration, while increasing the PEG concentration results in a noticeable decrease in the average pore diameter. This is likely due to denser packing within the acrylamide−PEG matrix at higher PEG loadings (Figure 3E).

The water absorption capacity of the DLHs was evaluated by measuring their swelling ratio over time, which showed a weight increase of approximately 106% (Figure S8). The FTIR spectra of PEG, DEX, ATPS, PEG-rich, and DEX-rich phases revealed distinct functional group contributions across the samples. The O−H stretching peak at 3325 cm^{-1} was observed in DEX and the DEX-rich phase, while the C−H stretching peak at 2879 cm^{-1} was observed in PEG and the PEG-rich phase. Similarly, the C−H bending vibration at 1467 cm^{-1} and the ether bond stretching peak at 1098 cm^{-1} were prominent

https://doi.org/10.1021/acsapm.5c01687
ACS Appl. Polym. Mater. 2025, 7, 10062−10073

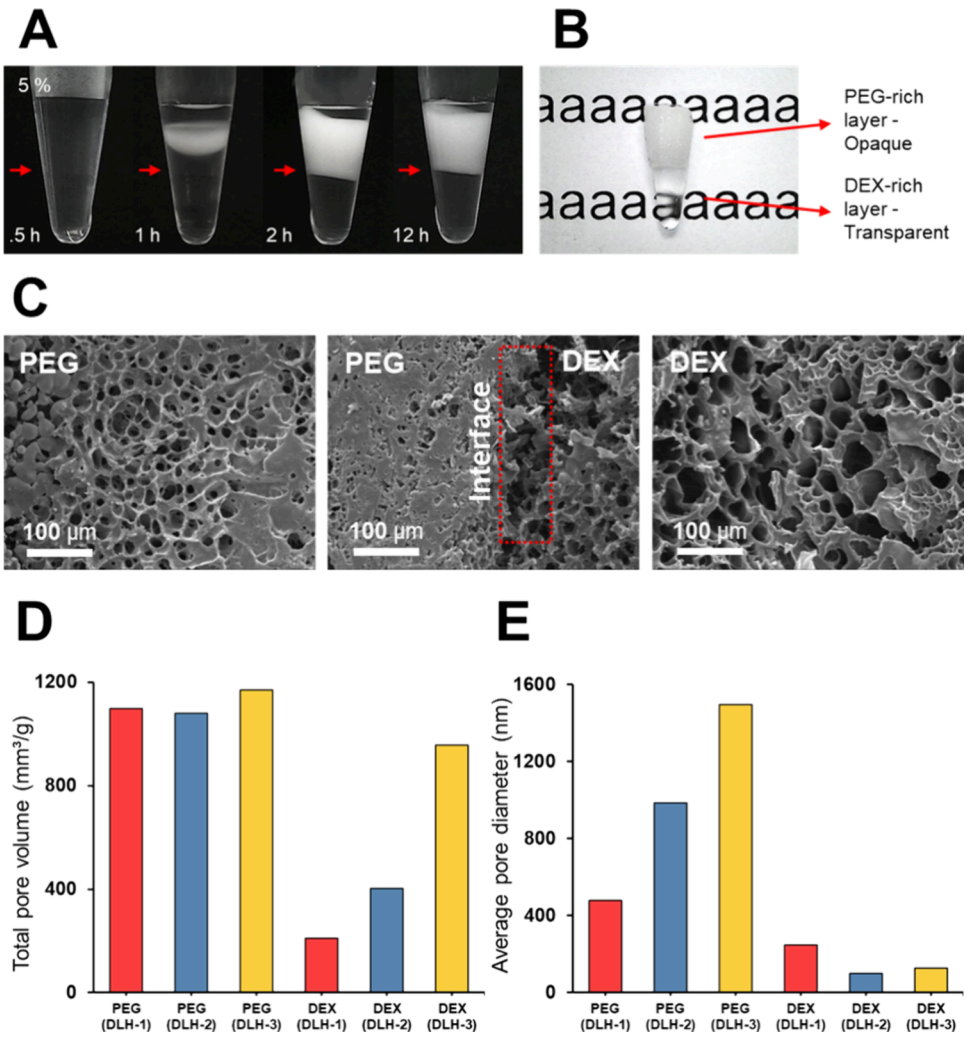

Figure 3. Polymerization of ATPS along with acrylamide/bis(acrylamide) (AA/BisAA) using Irgacure as a photoinitiator. (A) Digital images of time-dependent polymerization of ATPS with 5% Irgacure. (B) Visual comparison of the PEG-rich and DEX-rich hydrogel layers, highlighting the opacity of the PEG-rich layer and the transparency of the DEX-rich layer. (C) Scanning electron micrographs of the PEG-rich gel, interface between PEG-rich layer and DEX-rich layer, and DEX-rich gel containing 5% AA/BisAA. (D) Bar graph of total pore volume for PEG-rich and DEX-rich regions in DLH-1 to DLH-3. The DEX-rich phase shows a progressive increase in pore volume with increasing DEX concentration, while the PEG-rich phase maintains a relatively constant pore volume. (E) Bar graph of average pore diameter in PEG-rich and DEX-rich regions for DLH-1 to DLH-3. The PEG-rich phase consistently exhibits larger average pore diameters compared to the DEX-rich phase. A decrease in the pore diameter is observed in the DEX-rich phase with an increasing DEX concentration, while a similar trend is seen in the PEG-rich phase with an increasing PEG content.

in PEG and the PEG-rich phase compared to in DEX and the DEX-rich phase (Figure S9).[53]

We performed rheological analysis to further provide insights into the viscoelastic behavior of the DLHs. The variation of storage modulus (G') and loss modulus (G'') with varying strain amplitudes for the four different DLHs (DLH-1: PEG 8000 (10%) - DEX (4%), DLH-2: PEG 8000 (8%) - DEX (8%), DLH-3: PEG 8000 (4%) - DEX (12%), and DLH-4: PEG 400 (8%) - DEX (8%)) is shown in Figure 4A and Figure S10A–D. At lower strain amplitudes (<1%), all the DLHs exhibit a linear region where both the moduli remain constant. At strain amplitudes >7.5% (approx.), all the DLHs exhibit an overshoot in G''.[54] This is followed by a crossover in both G' and G'' at amplitudes closer to 10%, beyond which gels exhibit viscoelastic fluid-like response as G'' becomes greater than G'.[54,55] The frequency response of the four DLHs is shown in Figure 4B and Figure S10E–H. From the response, it can be observed that the storage modulus G' of the gels is nearly constant and is independent of the applied frequency, indicating the strong gel-like nature of the material systems.[55] The ability of the DLHs to recover after deformation was studied through 3iTT tests. Initially (time <120 s), the response is $G' > G''$, indicating viscoelastic solid-like response.[56] During load (or during deformation at higher strain amplitudes 120 s < time <180 s), the behavior is viscoelastic fluid-like as $G'' > G'$. However, when the load is removed again (time >180 s), the storage modulus G' of all the gels recovered back nearly to its original value, even after three cycles of loading (Figure S10I–L).[56] A 50 g object is placed on the ATPS hydrogel, causing the PEG-rich layer to deform, whereas the DEX-rich layer remains intact (Figure S11). The biocompatibility of the DLH was assessed by using an MTT assay on MDA-MB-231 cells, yielding a cell viability of approximately 80.55 ± 10.5%.

Following the characterization of Irgacure-polymerized DLHs with AA/BisAA, gold nanoparticles were incorporated

https://doi.org/10.1021/acsapm.5c01687
ACS Appl. Polym. Mater. 2025, 7, 10062–10073

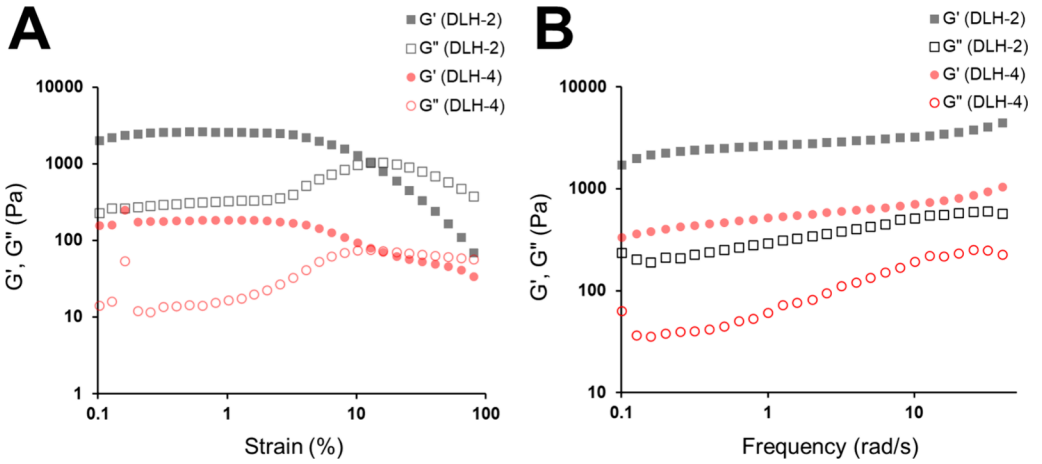

Figure 4. Rheological analysis of DLHs of varying molecular weights and compositions. DLH-2: PEG 8000 (8%) − DEX (8%), DLH-4: PEG 400 (8%) − DEX (8%). (A) Amplitude sweep response—variation of both storage (G') and loss (G'') moduli with varying strain amplitudes. (B) Frequency sweep response: variation of storage and loss modulus with varying angular frequencies.

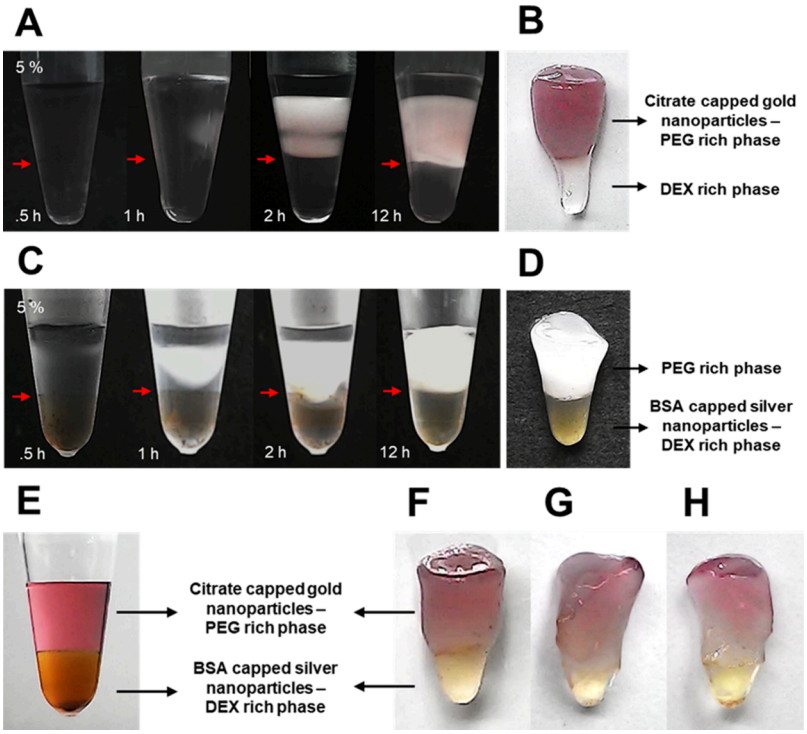

Figure 5. Polymerization of ATPS along with Nanoparticles. (A) Digital images of time-dependent polymerization of ATPS containing citrate-capped gold nanoparticles with 5% Irgacure, Polymerization was monitored at four different time intervals 0.5, 1, 2, and 12 h. (B) DLH embedded citrate-capped gold nanoparticles in the PEG-rich layer. (C) Digital images of time-dependent polymerization of ATPS containing BSA-capped silver nanoparticles with 5% Irgacure. Polymerization was monitored at four different time intervals 0.5, 1, 2, and 12 h. (D) DLH embedded with BSA-capped silver nanoparticles in the DEX-rich layer. (E) ATPS with citrate-capped gold nanoparticles in the PEG-rich top phase and BSA-capped silver nanoparticles in the DEX-rich bottom phase. (F) DLH embedded with citrate-capped gold nanoparticles in the PEG-rich top layer and BSA-capped silver nanoparticles in the DEX-rich bottom layer, respectively. (G, H) Sectioning along the vertical cross-sectional plane of the DLH revealed the presence of citrate-capped gold nanoparticles in the PEG-rich top layer and BSA-capped silver nanoparticles in the DEX-rich bottom layer.

into the system and the hydrogel was subjected to photopolymerization. The addition of Irgacure in the ATPS, AA/BisAA and gold nanoparticle system did not induce aggregation, as evidenced by the retention of the pink-colored dispersion of gold nanoparticles (Figure S12A). To investigate potential migration of gold nanoparticles due to gravitational settling or density differences, the system was left undisturbed for 12 h before initiating polymerization. No visible accumulation of nanoparticles at the interface was observed, confirming their stable localization within the PEG-rich layer (Figure S12A). Upon UV exposure, polymerization proceeded as expected, resulting in the formation of DLH with spatially confined gold nanoparticles in the PEG-rich phase (Figure 5A,B and Figure S12B). UV−visible spectroscopy analysis further confirmed nanoparticle stability with no significant shift

https://doi.org/10.1021/acsapm.5c01687
ACS Appl. Polym. Mater. 2025, 7, 10062−10073

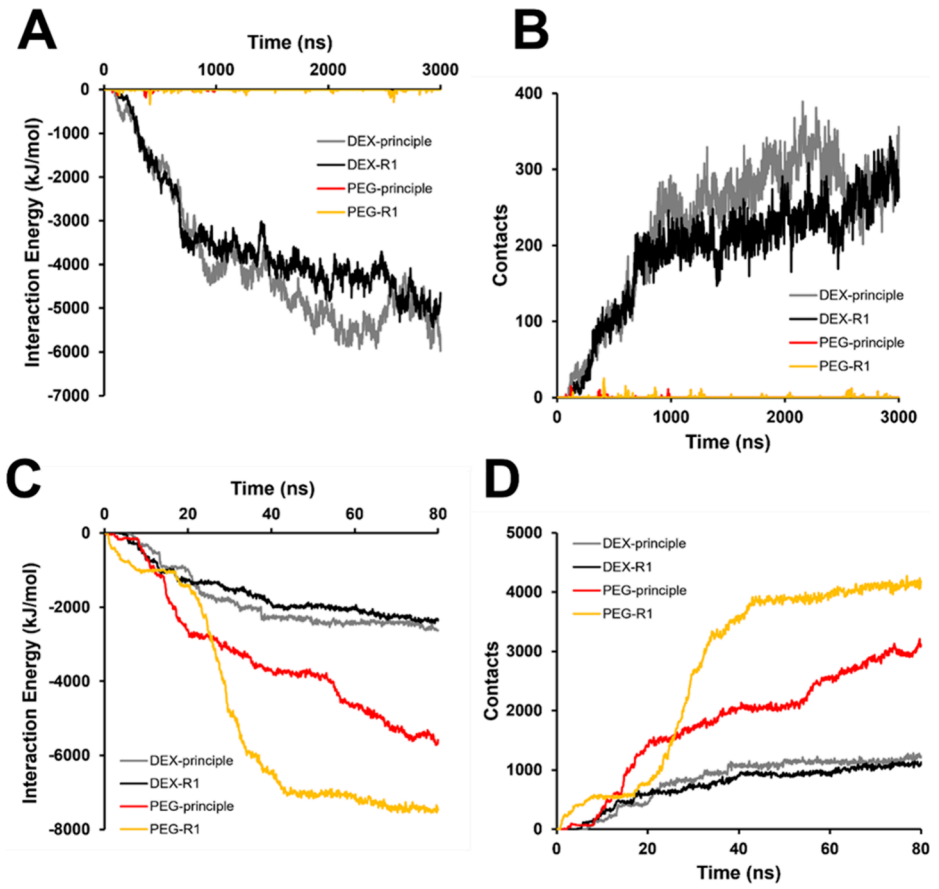

Figure 6. Molecular dynamics analysis for interactions of DEX and PEG with BSA and bare gold nanoparticle. (A) Interaction energy of DEX and PEG as a function of time with BSA. (B) The number of contacts between the BSA-DEX and BSA-PEG systems. (C) Interaction energy of DEX and PEG as a function of time with gold nanoparticles. (D) Number of contacts between gold nanoparticles-DEX and gold nanoparticles-PEG (principle refers to the first simulation performed, and R1 refers to its replication).

in the absorbance peak, indicating the absence of aggregation (Figure S12C).

To demonstrate the feasibility of introducing other nanoparticles into the alternate phase (DEX), we incorporated bovine serum albumin (BSA) into the ATPS mixture. This was guided by previous studies showing that native BSA partitioning in the PEG-DEX ATPS indicated a preferential partitioning in the DEX-rich phase over the PEG-rich phase.[57] We validated this through a ninhydrin assay, where a clear purple solution was seen in the DEX-rich phase, while the PEG-rich phase retained its transparent nature (Figure S13). Built on this, we synthesized silver nanoparticles capped with BSA. The synthesized silver nanoparticles were characterized for their size through TEM, indicating a diameter of 4.73 ± 2.15 nm (Figure S14). The zeta potential was measured as −17.529 ± 0.853 mV (pH 9). The BSA-capped silver nanoparticles were introduced into the ATPS, which clearly demonstrated their preferential migration to the DEX-rich phase (Figure S15A). We further quantified the presence of silver nanoparticles in each of the phases through UV−visible spectroscopy analysis by monitoring the absorbance at 450 nm, characteristic of silver nanoparticles (Figure S15B). The characteristic absorbance peak, observed in the DEX-rich phase, was absent in the PEG-rich phase (Figure S15B). The partition coefficient, defined as the ratio of absorbance in the PEG-rich phase to that in the DEX-rich phase, was found to be 0.094. Notably, there was no evidence of significant aggregation after the addition of Irgacure, as indicated by the absence of any wavelength shift, confirming the stability of the nanoparticles in the DEX-rich phase (Figure S16A,B). Subsequently, we photopolymerized the entire system for 2 h, which resulted in the generation of DLHs with clear localization of the BSA-capped silver nanoparticles in the DEX-rich phase (Figure 5C,D).

Finally, the fabrication of DLHs with citrate-capped gold nanoparticles in the PEG-rich phase and BSA-capped silver nanoparticles in the DEX-rich phase was successfully demonstrated through this process (Figure 5E,F). To validate the incorporation of nanoparticles, the DLH was sectioned along its vertical cross-sectional plane. Citrate-capped gold nanoparticles were observed within the PEG-rich top layer, while BSA-capped silver nanoparticles were distinctly visible in the DEX-rich bottom layer. These results confirm the effective encapsulation and spatial segregation of nanoparticles within the two hydrogel layers (Figure 5G,H).

To gain a molecular-level understanding of the interactions of gold nanoparticles favoring the PEG-rich phase while the BSA-coated silver nanoparticles favor the DEX-rich phase, we carried out molecular dynamics (MD) simulations. Figure 6A shows a comparison of the interaction energies between DEX and PEG with BSA. DEX exhibits a significantly stronger interaction with BSA, as indicated by its high negative interaction energy of −5136.3 kJ/mol as compared to −4.1 kJ/mol of PEG interaction with BSA. These results are

https://doi.org/10.1021/acsapm.5c01687
ACS Appl. Polym. Mater. 2025, 7, 10062−10073

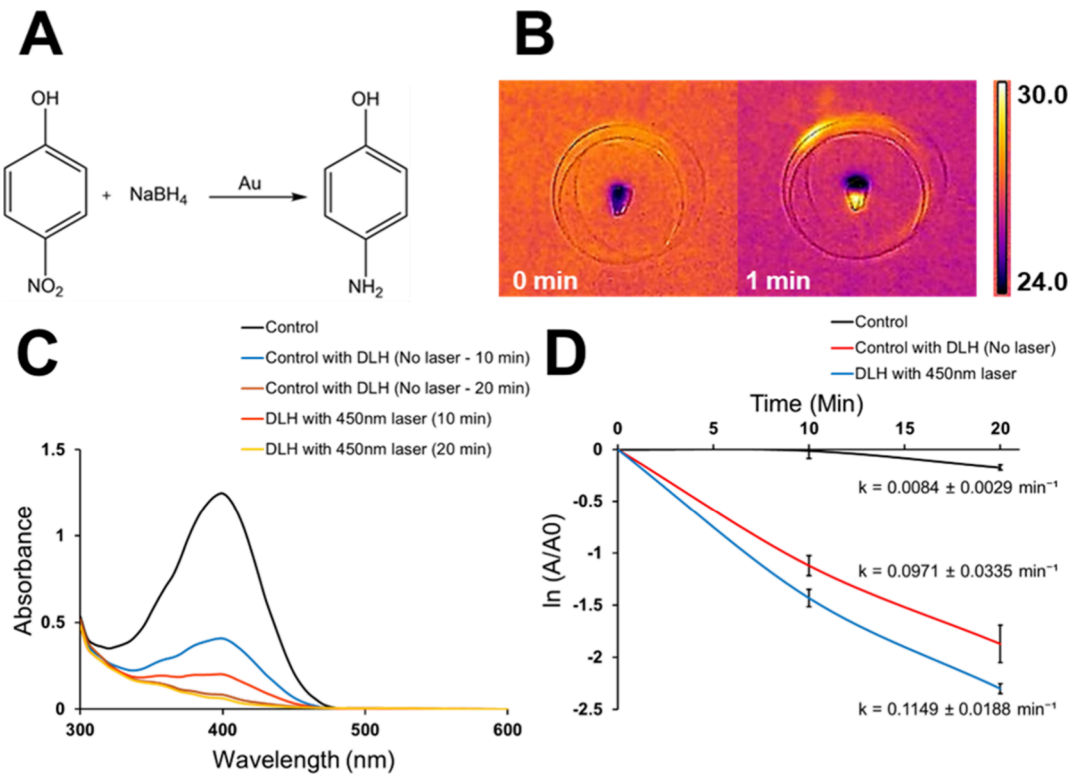

Figure 7. Laser-assisted catalytic reduction of *p*-nitrophenol (PNP) to *p*-aminophenol (PAP) using DLH embedded with gold and silver nanoparticles. (A) Reaction scheme of catalytic conversion of PNP to PAP with gold nanoparticles as the catalyst. (B) Infrared thermal image of the hydrogel under 450 nm laser irradiation, demonstrating localized photothermal heating induced by the embedded silver nanoparticles. (C) UV−vis absorbance spectroscopic analysis indicating the decrease in the PNP absorption peak at 400 nm over time, indicating conversion of PNP to PAP. (D) Plot of $\ln(A/A_0)$ versus reaction time (min) used to determine the rate constant of conversion of PNP to PAP (error bars represent standard deviations from triplicate measurements).

consistent with experimental findings. As anticipated, the number of contacts that DEX forms with BSA (∼290) is substantially greater than that made by PEG with BSA (∼0), reinforcing the experimental observation of preferential partitioning of BSA in the DEX phase (Figure 6B). This behavior can be attributed to the higher number of hydrophilic contacts between DEX and BSA, while hydrophobic contacts remain minimal (Figure S17A).

In contrast, simulations of gold nanoparticles in PEG and DEX environments reveal the opposite trend: the gold nanoparticle shows a stronger interaction with PEG than with DEX, as reflected by its more negative interaction energy (−6473.52 kJ/mol for PEG vs −2452.5 kJ/mol for DEX) and a higher number of contacts (∼3550 for PEG vs ∼1150 for DEX) (Figure 6C,D). Additionally, the PEG molecule consists of 1270 atoms, including 82 oxygen, 362 carbon, and 726 hydrogen atoms. The number of contacts for each atom type is plotted separately in Figure S17B, showing that the entire PEG molecule contributes to binding. To further probe the role of citrate in modulating these interactions, we performed separate simulations of PEG and DEX trimers in the presence of deprotonated monocitrate molecule alone, without gold nanoparticles. These revealed a minimal interaction between either polymer or citrate, with no significant preference of PEG (−0.014 kJ/mol) over DEX (−0.29 kJ/mol) (Figure S18). This is indicative of PEG's preferential interaction with gold nanoparticles from its direct association with the gold surface rather than with citrate.

Finally, we seek to establish the catalytic ability of the DLHs by demonstrating its ability to mediate the catalytic reduction of *p*-nitrophenol (PNP) to *p*-aminophenol (PAP) using sodium borohydride ($NaBH_4$), which proceeds through a well-established mechanism facilitated by gold nanoparticles.[58,59] In this reaction, both PNP and BH_4^- ions adsorb onto the surface of the gold nanoparticles.[58,59] The nanoparticles act as electron transfer mediators, enabling the transfer of electrons from the BH_4^- donor to the PNP.[59] This electron transfer leads to the reduction of the nitro group ($-NO_2$) to an amino group ($-NH_2$), resulting in the formation of PAP. Throughout the process, the gold nanoparticles serve as the catalyst (Figure 7A).[60] Additionally, we hypothesized that exposure of a 450 nm laser to DLH would induce a photothermal effect due to the absorption of the laser through silver nanoparticles. We posit that this temperature change will result in the enhancement of the rate kinetics of the reduction of PNP. To validate the temperature rise due to laser exposure, thermal images were acquired with photoexposure. After 1 min of irradiation, a clear rise in temperature to ∼30 °C in the bottom DEX-rich layer containing silver nanoparticles is observed while the top PEG-rich layer containing gold nanoparticles remains at a lower temperature (∼24 °C) (Figure 7B and Figure S19). After 5 min of radiation, both layers exhibit a uniform temperature (∼31.5 °C), highlighting heat propagation through the hydrogel (Figure S19).

We further evaluated the catalytic reduction of PNP to PAP under three conditions. The progression of the reaction was

https://doi.org/10.1021/acsapm.5c01687
ACS Appl. Polym. Mater. 2025, 7, 10062−10073

monitored by tracking the decrease in the characteristic absorption peak of the PNP at 400 nm. In the first control, only PNP and $NaBH_4$ were used without the DLH or laser, showing negligible reduction (Figure 7C). In the second control, the reaction mixture included the DLH containing gold and silver nanoparticles but no laser was applied, resulting in catalytic activity (Figure 7C). In the third condition, the reaction mixture included DLH containing gold and silver nanoparticles exposed to a 450 nm laser, leading to an enhanced decrease in absorbance over time (Figure 7C). This confirms enhanced catalytic activity due to the laser-induced activation of silver nanoparticles in the DEX-rich layer, which in turn boosts the catalytic efficiency of gold nanoparticles in the PEG-rich layer (Figure 7C). The rate constant (k) for the reaction was calculated with a pseudo-first-order kinetic model, given the excess concentration of $NaBH_4$. A linear plot of $\ln(A/A_0)$ versus time (min), where A is the absorbance at a given time, and A_0 is the initial absorbance, was used to determine the value of k (Figure 7D). A clear increase in the rate constant from 0.0084 ± 0.0029 min^{-1} (control), 0.0971 ± 0.0335 min^{-1} (control with DLH−no laser) to 0.1149 ± 0.0188 min^{-1} in the presence of the laser highlights the functionality of the silver layer in heat generation while the gold layer facilitates the catalysis (Figure 7D). We anticipate that this approach will provide a more efficient and streamlined method for fabricating DLHs, offering precise control over nanoparticle localization and opening new possibilities for diverse applications.

CONCLUSIONS

This study presents an approach for synthesizing dual-layered hydrogels (DLHs) with tailored nanoparticles in each layer through an aqueous two-phase system (ATPS) by seamlessly integrating phase separation, nanoparticle localization, and polymerization. Polyethylene glycol (PEG) and dextran (DEX) were used to generate dual-layered aqueous phases, while acrylamide, bis(acrylamide), and ammonium persulfate (APS) were utilized to fabricate hydrogels within each phase. However, while citrate-capped gold nanoparticles preferentially migrated to the PEG-rich phase, the ionizable groups in APS caused nanoparticle aggregation. To address this, we adopted Irgacure, a nonionizable initiator activated by exposure to 395 nm light. ATPS hydrogels fabricated with varying Irgacure concentrations (1 and 5%) were characterized through SEM analysis, which revealed that higher AA/BisAA concentrations (10%) resulted in smaller and uniform pores compared to the larger and less uniform pores in their 5% AA/BisAA counterparts. Rheological analysis confirmed that all DLHs exhibited predominantly elastic behavior in the linear viscoelastic region (<1% strain), with a $G' > G''$ profile. At higher strains (~10%), a crossover occurred, indicating a transition to fluid-like behavior. Mercury intrusion porosimetry revealed that the PEG-rich phase had higher total pore volume and larger average pore diameter compared to the DEX-rich phase. As hypothesized, the use of Irgacure preserved the colloidal stability of citrate-capped gold nanoparticles while enabling the formation of DLHs. Alternatively, BSA-capped silver nanoparticles exhibited a preferential affinity for the DEX-rich phase. Ultimately, we successfully fabricated DLHs with citrate-capped gold nanoparticles localized in the PEG-rich phase and BSA-capped silver nanoparticles in the DEX-rich phase. Furthermore, catalytic dye degradation studies validated the system's functional utility—laser activation of silver nanoparticles in the DEX-rich phase enhanced the gold nanoparticle-catalyzed reduction of p-nitrophenol, as evidenced by higher reaction rate constants. We anticipate that this ATPS-based fabrication approach overcomes the challenges associated with multistep synthesis, offering a scalable, efficient, and reproducible method for creating advanced hybrid materials.

ASSOCIATED CONTENT

Supporting Information

The Supporting Information is available free of charge at https://pubs.acs.org/doi/10.1021/acsapm.5c01687.

Polymerization of an aqueous two-phase system (ATPS) using ammonium persulfate (APS); transmission electron micrographs of gold nanoparticles; influence of PEG and DEX weight percentages on gold nanoparticle localization in ATPS; polymerization of ATPS using Irgacure as polymerization photoinitiator; polymerization of ATPS along with acrylamide/Bis(acrylamide) using Irgacure as photoinitiator; scanning electron micrographs; differential intrusion curves and porosity analysis of DLHs; time-dependent swelling behavior of DLHs; Fourier transform infrared (FTIR) spectra; rheological analysis of four different DLHs of varying molecular weights and compositions; deformation of the DLH under load; interaction of gold nanoparticles with Irgacure photoinitiator; preferential partitioning of BSA protein into the DEX-rich layer over the PEG-rich layer in ATPS; size characterization of BSA-capped silver nanoparticles; ATPS with BSA-capped silver nanoparticle distribution and absorbance studies; interaction of BSA-capped silver nanoparticles with Irgacure photoinitiator; number of contacts; interaction energies of trimers of DEX and PEG with deprotonated monocitrate; infrared thermal imaging of DLH under 450 nm laser irradiation; and photothermal response over time (PDF)

AUTHOR INFORMATION

Corresponding Author

Karthik Pushpavanam − *Chemical Engineering, IIT Gandhinagar, Gujarat 382055, India;* orcid.org/0000-0001-6312-2572; Phone: +917923952587; Email: kpsubram@iitgn.ac.in

Authors

Aniruddha Kambekar − *Chemical Engineering, IIT Gandhinagar, Gujarat 382055, India;* orcid.org/0000-0001-7190-6772

Vignesh Nandhagopal − *Chemical Engineering, IIT Gandhinagar, Gujarat 382055, India*

Aditya Mehta − *Chemical Engineering, IIT Gandhinagar, Gujarat 382055, India*

Yashwant Kumar − *Chemical Engineering, IIT Gandhinagar, Gujarat 382055, India*

Reman Kumar Singh − *Department of Chemistry, St. Xavier's College, Ranchi, Jharkhand 834001, India;* orcid.org/0000-0001-6160-4586

Complete contact information is available at: https://pubs.acs.org/10.1021/acsapm.5c01687

https://doi.org/10.1021/acsapm.5c01687
ACS Appl. Polym. Mater. 2025, 7, 10062−10073

Author Contributions

The original idea, research concept, and experimental design were developed by K.P. A.K. carried out the experiments and data analyses. V.N. and A.M. carried out molecular simulations and their analysis, and R.K.S. supervised the molecular simulations and their analysis. Y.K. provided feedback and helped shape the analysis and the manuscript. K.P. supervised the overall research and provided critical feedback during manuscript writing. K.P. is thankful to the Department of Biotechnology BT/PR45697/BCE/8/1797/2023 for the project funding.

Notes

The authors declare no competing financial interest.

■ ACKNOWLEDGMENTS

The authors would like to sincerely thank IIT Gandhinagar for providing the facilities and resources necessary to carry out this study. We thank CIF (Central Instrumentation Facility), CRTDH (Common Resource and Technology Development Hub) for the instrumentation facilities, the Nanoplasmonics Lab (Professor Saumyakanti Khatua, Dr. NVS Praneeth) for the laser facility, Dr. Abhijit P. Deshpande and Saveri Puchalapalli from IIT Madras for the Rheology studies, Ms. Manavi from IIT Madras for the Mercury Intrusion Porosimetry analysis, and Mr. Jaydeep Kanungo for the Biocompatibility studies. We thank the PARAMANANTA Supercomputing facility for running the molecular dynamics simulations. OpenAI ChatGPT and Perplexity AI were used for rephrasing and grammar corrections in the manuscript.

■ REFERENCES

(1) Ho, T.-C.; Chang, C.-C.; Chan, H.-P.; Chung, T.-W.; Shu, C.-W.; Chuang, K.-P.; Duh, T.-H.; Yang, M.-H.; Tyan, Y.-C. Hydrogels: Properties and Applications in Biomedicine. *Molecules* **2022**, *27* (9), No. 2902.

(2) Ahmed, E. M. Hydrogel: Preparation, Characterization, and Applications: A Review. *J. Adv. Res.* **2015**, *6* (2), 105−121.

(3) Patra, P.; Upadhyay, T. K.; Alshammari, N.; Saeed, M.; Kesari, K. K. Alginate-Chitosan Biodegradable and Biocompatible Based Hydrogel for Breast Cancer Immunotherapy and Diagnosis: A Comprehensive Review. *ACS Appl. Bio Mater.* **2024**, *7* (6), 3515−3534.

(4) Davoodi, P.; Ng, W. C.; Srinivasan, M. P.; Wang, C. Codelivery of Anti-cancer Agents via Double-walled Polymeric Microparticles/Injectable Hydrogel: A Promising Approach for Treatment of Triple Negative Breast Cancer. *Biotechnol. Bioeng.* **2017**, *114* (12), 2931−2946.

(5) McKenzie, M.; Betts, D.; Suh, A.; Bui, K.; Kim, L.; Cho, H. Hydrogel-Based Drug Delivery Systems for Poorly Water-Soluble Drugs. *Molecules* **2015**, *20* (11), 20397−20408.

(6) Madurantakam, P. A.; Cost, C. P.; Simpson, D. G.; Bowlin, G. L. Science of Nanofibrous Scaffold Fabrication: Strategies for Next Generation Tissue-Engineering Scaffolds. *Nanomedicine* **2009**, *4* (2), 193−206.

(7) Iqbal, M.; Tao, Y.; Xie, S.; Zhu, Y.; Chen, D.; Wang, X.; Huang, L.; Peng, D.; Sattar, A.; Shabbir, M. A. B.; Hussain, H. I.; Ahmed, S.; Yuan, Z. Aqueous Two-Phase System (ATPS): An Overview and Advances in Its Applications. *Biol. Proced Online* **2016**, *18* (1), 18.

(8) Khan, I.; Saeed, K.; Khan, I. Nanoparticles: Properties, Applications and Toxicities. *Arabian Journal of Chemistry* **2019**, *12* (7), 908−931.

(9) Ziai, Y.; Rinoldi, C.; Nakielski, P.; De Sio, L.; Pierini, F. Smart Plasmonic Hydrogels Based on Gold and Silver Nanoparticles for Biosensing Application. *Curr. Opin Biomed Eng.* **2022**, *24*, No. 100413.

(10) Kaul, A. The Phase Diagram. In *Aqueous Two-Phase Systems*; Humana Press: NJ, pp 11−21. .

(11) Feng, A.; Onggowarsito, C.; Mao, S.; Qiao, G. G.; Fu, Q. Divide and Conquer: A Novel Dual-Layered Hydrogel for Atmospheric Moisture Harvesting. *ChemSusChem* **2023**, *16* (14), No. e202300137.

(12) Lee, W. H.; Lee, C. W.; Cha, G. D.; Lee, B.-H.; Jeong, J. H.; Park, H.; Heo, J.; Bootharaju, M. S.; Sunwoo, S.-H.; Kim, J. H.; Ahn, K. H.; Kim, D.-H.; Hyeon, T. Floatable Photocatalytic Hydrogel Nanocomposites for Large-Scale Solar Hydrogen Production. *Nat. Nanotechnol* **2023**, *18* (7), 754−762.

(13) Liu, G.; Ding, Z.; Yuan, Q.; Xie, H.; Gu, Z. Multi-Layered Hydrogels for Biomedical Applications. *Front Chem.* **2018**, *6*, 439.

(14) Yan, T.; Cheng, J.; Liu, H.; Wang, Y.; Zhang, C.; Huang, D.; Liu, J.; Wang, Z. Multifunctional Janus Hydrogels: Surface Design Strategies for Next-Generation Clinical Solutions. *Gels* **2025**, *11* (5), No. 343.

(15) Wu, P.; Zhou, H.; Gao, Y.; Chen, Y.; Wang, K.; Wei, C.; Zhang, H.; Jin, X.; Ma, A.; Chen, W.; Liu, H. Double Layered Asymmetrical Hydrogels Enhanced by Thermosensitive Microgels for High-Performance Mechanosensors and Actuators. *J. Colloid Interface Sci.* **2024**, *662*, 976−985.

(16) Bruchet, M.; Melman, A. Fabrication of Patterned Calcium Cross-Linked Alginate Hydrogel Films and Coatings through Reductive Cation Exchange. *Carbohydr. Polym.* **2015**, *131*, 57−64.

(17) Sadik, W. A.-A.; El-Demerdash, A.-G. M.; Abbas, R.; Gabre, H. A. Fast Synthesis of an Eco-Friendly Starch-Grafted Poly(N, N-Dimethyl Acrylamide) Hydrogel for the Removal of Acid Red 8 Dye from Aqueous Solutions. *Polym. Bull.* **2020**, *77* (8), 4445−4468.

(18) Hu, Y.; Hu, S.; Zhang, S.; Dong, S.; Hu, J.; Kang, L.; Yang, X. A Double-Layer Hydrogel Based on Alginate-Carboxymethyl Cellulose and Synthetic Polymer as Sustained Drug Delivery System. *Sci. Rep* **2021**, *11* (1), 9142.

(19) Chen, F.; Li, X.; Yu, Y.; Li, Q.; Lin, H.; Xu, L.; Shum, H. C. Phase-Separation Facilitated One-Step Fabrication of Multiscale Heterogeneous Two-Aqueous-Phase Gel. *Nat. Commun.* **2023**, *14* (1), 2793.

(20) Kimling, J.; Maier, M.; Okenve, B.; Kotaidis, V.; Ballot, H.; Plech, A. Turkevich Method for Gold Nanoparticle Synthesis Revisited. *J. Phys. Chem. B* **2006**, *110* (32), 15700−15707.

(21) Wang, J.; Zhao, J.; Ma, G. Extremely Concentrated Silver Nanoparticles Stabilized in Aqueous Solution by Bovine Serum Albumin (BSA). *Nano-Structures & Nano-Objects* **2019**, *19*, No. 100349.

(22) Jumper, J.; Evans, R.; Pritzel, A.; Green, T.; Figurnov, M.; Ronneberger, O.; Tunyasuvunakool, K.; Bates, R.; Žídek, A.; Potapenko, A.; Bridgland, A.; Meyer, C.; Kohl, S. A. A.; Ballard, A. J.; Cowie, A.; Romera-Paredes, B.; Nikolov, S.; Jain, R.; Adler, J.; Back, T.; Petersen, S.; Reiman, D.; Clancy, E.; Zielinski, M.; Steinegger, M.; Pacholska, M.; Berghammer, T.; Bodenstein, S.; Silver, D.; Vinyals, O.; Senior, A. W.; Kavukcuoglu, K.; Kohli, P.; Hassabis, D. Highly Accurate Protein Structure Prediction with AlphaFold. *Nature* **2021**, *596* (7873), 583−589.

(23) Grünewald, F.; Alessandri, R.; Kroon, P. C.; Monticelli, L.; Souza, P. C. T.; Marrink, S. J. Polyply; a Python Suite for Facilitating Simulations of Macromolecules and Nanomaterials. *Nat. Commun.* **2022**, *13* (1), 68.

(24) Periole, X.; Cavalli, M.; Marrink, S.-J.; Ceruso, M. A. Combining an Elastic Network With a Coarse-Grained Molecular Force Field: Structure, Dynamics, and Intermolecular Recognition. *J. Chem. Theory Comput* **2009**, *5* (9), 2531−2543.

(25) Kroon, P.; Grunewald, F.; Barnoud, J.; van Tilburg, M.; Souza, P.; Wassenaar, T.; Marrink, S. Martinize2 and Vermouth: Unified Framework for Topology Generation. *arXiv e-prints* **2024**.

(26) Souza, P. C. T.; Alessandri, R.; Barnoud, J.; Thallmair, S.; Faustino, I.; Grünewald, F.; Patmanidis, I.; Abdizadeh, H.; Bruininks, B. M. H.; Wassenaar, T. A.; Kroon, P. C.; Melcr, J.; Nieto, V.; Corradi, V.; Khan, H. M.; Domański, J.; Javanainen, M.; Martinez-Seara, H.; Reuter, N.; Best, R. B.; Vattulainen, I.; Monticelli, L.; Periole, X.; Tieleman, D. P.; de Vries, A. H.; Marrink, S. J. Martini 3:

https://doi.org/10.1021/acsapm.5c01687
ACS Appl. Polym. Mater. 2025, 7, 10062−10073

A General Purpose Force Field for Coarse-Grained Molecular Dynamics. *Nat. Methods* **2021**, *18* (4), 382−388.
(27) Bussi, G.; Donadio, D.; Parrinello, M. Canonical Sampling through Velocity Rescaling. *J. Chem. Phys.* **2007**, *126* (1), No. 014101.
(28) Berendsen, H. J. C.; van der Spoel, D.; van Drunen, R. GROMACS: A Message-Passing Parallel Molecular Dynamics Implementation. *Comput. Phys. Commun.* **1995**, *91* (1−3), 43−56.
(29) Parrinello, M.; Rahman, A. Polymorphic Transitions in Single Crystals: A New Molecular Dynamics Method. *J. Appl. Phys.* **1981**, *52* (12), 7182−7190.
(30) Abraham, M. J.; Murtola, T.; Schulz, R.; Páll, S.; Smith, J. C.; Hess, B.; Lindahl, E. GROMACS: High Performance Molecular Simulations through Multi-Level Parallelism from Laptops to Supercomputers. *SoftwareX* **2015**, *1−2*, 19−25.
(31) Hess, B.; Bekker, H.; Berendsen, H. J. C.; Fraaije, J. G. E. M. LINCS: A Linear Constraint Solver for Molecular Simulations. *J. Comput. Chem.* **1997**, *18* (12), 1463−1472.
(32) Jo, S.; Kim, T.; Iyer, V. G.; Im, W. CHARMM-GUI: A Web-based Graphical User Interface for CHARMM. *J. Comput. Chem.* **2008**, *29* (11), 1859−1865.
(33) Brooks, B. R.; Brooks, C. L.; Mackerell, A. D.; Nilsson, L.; Petrella, R. J.; Roux, B.; Won, Y.; Archontis, G.; Bartels, C.; Boresch, S.; Caflisch, A.; Caves, L.; Cui, Q.; Dinner, A. R.; Feig, M.; Fischer, S.; Gao, J.; Hodoscek, M.; Im, W.; Kuczera, K.; Lazaridis, T.; Ma, J.; Ovchinnikov, V.; Paci, E.; Pastor, R. W.; Post, C. B.; Pu, J. Z.; Schaefer, M.; Tidor, B.; Venable, R. M.; Woodcock, H. L.; Wu, X.; Yang, W.; York, D. M.; Karplus, M. CHARMM: The Biomolecular Simulation Program. *J. Comput. Chem.* **2009**, *30* (10), 1545−1614.
(34) Lee, J.; Cheng, X.; Swails, J. M.; Yeom, M. S.; Eastman, P. K.; Lemkul, J. A.; Wei, S.; Buckner, J.; Jeong, J. C.; Qi, Y.; Jo, S.; Pande, V. S.; Case, D. A.; Brooks, C. L.; MacKerell, A. D.; Klauda, J. B.; Im, W. CHARMM-GUI Input Generator for NAMD, GROMACS, AMBER, OpenMM, and CHARMM/OpenMM Simulations Using the CHARMM36 Additive Force Field. *J. Chem. Theory Comput* **2016**, *12* (1), 405−413.
(35) Choi, Y. K.; Kern, N. R.; Kim, S.; Kanhaiya, K.; Afshar, Y.; Jeon, S. H.; Jo, S.; Brooks, B. R.; Lee, J.; Tadmor, E. B.; Heinz, H.; Im, W. CHARMM-GUI Nanomaterial Modeler for Modeling and Simulation of Nanomaterial Systems. *J. Chem. Theory Comput* **2022**, *18* (1), 479−493.
(36) Choi, Y. K.; Park, S.-J.; Park, S.; Kim, S.; Kern, N. R.; Lee, J.; Im, W. CHARMM-GUI Polymer Builder for Modeling and Simulation of Synthetic Polymers. *J. Chem. Theory Comput* **2021**, *17* (4), 2431−2443.
(37) Jo, S.; Song, K. C.; Desaire, H.; MacKerell, A. D.; Im, W. Glycan Reader: Automated Sugar Identification and Simulation Preparation for Carbohydrates and Glycoproteins. *J. Comput. Chem.* **2011**, *32* (14), 3135−3141.
(38) Park, S.-J.; Lee, J.; Patel, D. S.; Ma, H.; Lee, H. S.; Jo, S.; Im, W. Glycan Reader Is Improved to Recognize Most Sugar Types and Chemical Modifications in the Protein Data Bank. *Bioinformatics* **2017**, *33* (19), 3051−3057.
(39) Park, S.-J.; Lee, J.; Qi, Y.; Kern, N. R.; Lee, H. S.; Jo, S.; Joung, I.; Joo, K.; Lee, J.; Im, W. CHARMM-GUI *Glycan Modeler* for Modeling and Simulation of Carbohydrates and Glycoconjugates. *Glycobiology* **2019**, *29* (4), 320−331.
(40) Kirkpatrick, S.; Gelatt, C. D.; Vecchi, M. P. Optimization by Simulated Annealing. *Science (1979)* **1983**, *220* (4598), 671−680.
(41) Jorgensen, W. L.; Chandrasekhar, J.; Madura, J. D.; Impey, R. W.; Klein, M. L. Comparison of Simple Potential Functions for Simulating Liquid Water. *J. Chem. Phys.* **1983**, *79* (2), 926−935.
(42) Darden, T.; York, D.; Pedersen, L. Particle Mesh Ewald: An $N \cdot \log(N)$ Method for Ewald Sums in Large Systems. *J. Chem. Phys.* **1993**, *98* (12), 10089−10092.
(43) Ao, G.; Khripin, C. Y.; Zheng, M. DNA-Controlled Partition of Carbon Nanotubes in Polymer Aqueous Two-Phase Systems. *J. Am. Chem. Soc.* **2014**, *136* (29), 10383−10392.
(44) Kinhal, K. V.; Sinha, S.; Ravisankar, A.; Bhatt, N. P.; Pushpavanam, S. Simultaneous Synthesis and Separation of Nanoparticles Using Aqueous Two-Phase Systems. *ACS Sustain Chem. Eng.* **2020**, *8* (7), 3013−3025.
(45) Zhou, Y.-J.; Hu, C.-L.; Wang, N.; Zhang, W.-W.; Yu, X.-Q. Purification of Porcine Pancreatic Lipase by Aqueous Two-Phase Systems of Polyethylene Glycol and Potassium Phosphate. *Journal of Chromatography B* **2013**, *926*, 77−82.
(46) Senphan, T.; Benjakul, S. Use of the Combined Phase Partitioning Systems for Recovery of Proteases from Hepatopancreas of Pacific White Shrimp. *Sep Purif Technol.* **2014**, *129*, 57−63.
(47) Christau, S.; Moeller, T.; Genzer, J.; Koehler, R.; von Klitzing, R. Salt-Induced Aggregation of Negatively Charged Gold Nanoparticles Confined in a Polymer Brush Matrix. *Macromolecules* **2017**, *50* (18), 7333−7343.
(48) Almagro-Gómez, C. M.; Ortuño, J. Á.; de la Torre, J. G.; Hernandez-Cifre, J. G. Effect of Large Ammonium Cations on the Aggregation Kinetics of Citrate Capped Gold Nanoparticles. *J. Nanopart. Res.* **2023**, *25* (9), 175.
(49) Tomal, W.; Ortyl, J. *Water-Soluble Photoinitiators in Biomedical Applications. Polymers (Basel)* **2020**, *12* (5), No. 1073.
(50) Hirata, Y.; Aoki, M.; Kobatake, H.; Yamamoto, H. Insolubilization of Water-Soluble Dextran. *Biomaterials* **1999**, *20* (4), 303−307.
(51) Stenekes, R. J. H.; Talsma, H.; Hennink, W. E. Formation of Dextran Hydrogels by Crystallization. *Biomaterials* **2001**, *22* (13), 1891−1898.
(52) Djabourov, M.; Bouchemal, K. Polymer Gels, Hydrogels, and Scaffolds − An Overview. In *Disordered Pharmaceutical Materials*; Wiley, 2016; pp 241−282. .
(53) Fadlelmoula, A.; Pinho, D.; Carvalho, V. H.; Catarino, S. O.; Minas, G. Fourier Transform Infrared (FTIR) Spectroscopy to Analyse Human Blood over the Last 20 Years: A Review towards Lab-on-a-Chip Devices. *Micromachines (Basel)* **2022**, *13* (2), No. 187.
(54) Li, Q.; Xu, M.; Xie, J.; Su, E.; Wan, Z.; Sagis, L. M. C.; Yang, X. Large Amplitude Oscillatory Shear (LAOS) for Nonlinear Rheological Behavior of Heterogeneous Emulsion Gels Made from Natural Supramolecular Gelators. *Food Research International* **2021**, *140*, No. 110076.
(55) Stojkov, G.; Niyazov, Z.; Picchioni, F.; Bose, R. K. Relationship between Structure and Rheology of Hydrogels for Various Applications. *Gels* **2021**, *7* (4), No. 255.
(56) Toker, O. S.; Karasu, S.; Yilmaz, M. T.; Karaman, S. Three Interval Thixotropy Test (3ITT) in Food Applications: A Novel Technique to Determine Structural Regeneration of Mayonnaise under Different Shear Conditions. *Food Research International* **2015**, *70*, 125−133.
(57) Long, M. S.; Keating, C. D. Nanoparticle Conjugation Increases Protein Partitioning in Aqueous Two-Phase Systems. *Anal. Chem.* **2006**, *78* (2), 379−386.
(58) Gangula, A.; Podila, R.; M, R.; Karanam, L.; Janardhana, C.; Rao, A. M. Catalytic Reduction of 4-Nitrophenol Using Biogenic Gold and Silver Nanoparticles Derived from *Breynia Rhamnoides*. *Langmuir* **2011**, *27* (24), 15268−15274.
(59) Ismail, A. A.; Hakki, A.; Bahnemann, D. W. Mesostructure Au/TiO2 Nanocomposites for Highly Efficient Catalytic Reduction of p-Nitrophenol. *J. Mol. Catal. A Chem.* **2012**, *358*, 145−151.
(60) Lomonosov, V.; Asselin, J.; Ringe, E. Solvent Effects on the Kinetics of 4-Nitrophenol Reduction by $NaBH_4$ in the Presence of Ag and Au Nanoparticles. *React. Chem. Eng.* **2022**, *7* (8), 1728−1741.